



A new integration algorithm for finite strain J_2 plasticity based on midpoint rule

M. Jahanshahi*

Department of Civil Engineering, School of Science and Engineering, Sharif University of Technology, International Campus, Kish Island, P.O. Box 76417-76655, Iran.

Received 8 September 2013; received in revised form 14 September 2014; accepted 1 December 2014

KEYWORDS

Plasticity;
 Backward Euler method;
 Midpoint rule;
 Finite strain;
 Tangent operator;
 Isotropic and kinematic hardening.

Abstract. Integrating the rate form equations governing the behavior of material is an important step in solving every plasticity problem. Providing a compromise between accuracy and computational effort demands the combination of low order elements with efficient integration algorithms. First and second order accurate integration algorithms are well established in the realm of infinitesimal theory. However for large deformation plasticity models, second order integration algorithms are not given much attention in the literature. Inspired by midpoint rule algorithms conventionally used in small deformations, a new integration algorithm is proposed for finite strain J_2 plasticity that outperforms the classical backward Euler method. Algorithmic setup as well as the derivation of tangent operator which is crucial for quadratic rate of convergence of the Newton-Raphson algorithm is discussed in detail. Employing four node quadrilateral elements in solving benchmark examples it is shown that the proposed algorithm is very stable from numerical standpoint and has outstanding convergence properties.

© 2015 Sharif University of Technology. All rights reserved.

1. Introduction

It seems that the roots of integration algorithms for small deformation plasticity can be found in the work of Wilkins [1]. The algorithm that he developed was actually a backward Euler type of algorithm. Midpoint rule algorithms were introduced by Ortiz and Popov [2]. Ortiz and Simo also presented a method for analyzing the stability of integration algorithms [3]. The double step algorithms with consistency condition being enforced twice per time step were introduced by Simo [4] but were not elaborated until recently. Artioli et al. provided a detailed development and numerical results for different types of second order integration algorithms with general isotropic and linear kinematic hardening [5]. Jahanshahi presented comparisons and discussions on relative efficiency of these types of algorithms [6]. He also extended a variant of double step

integration algorithm for nonlinear kinematic hardening [7]. In addition to previous integration techniques, Runge Kutta methods with step size control have been used efficiently by Hartmann et al. to deal with governing rate form equations as differential-algebraic equations [8-10].

In finite strain regime, the algorithms that are used to deal with plasticity problems are roughly divided into hypoelastic and hyperelastic based algorithms [11,12]. In the first group, the governing equations are expressed with respect to a rotation neutral configuration and the tangent operator is assumed to be constant. Despite the shortcomings of hypoelasticity, it is widely used in large scale computations [13-19]. On the other hand, the algorithms in the second group are formulated with respect to an intermediate configuration relative to which the elastic behavior of material can be characterized [20,11]. The assumption of intermediate configuration first introduced by Lee [21] is motivated by the micromechanical behavior of a single

*. E-mail address: jahanshahi@sharif.edu (M. Jahanshahi)

crystal in metal plasticity and leads to a multiplicative decomposition of the deformation gradient into elastic and plastic parts [11,12]. Unlike hypoelasticity, hyperelastic algorithms can be linearized and tangent operators consistent with algorithmic setup can be computed in closed form. The stress-strain relationship derives from a potential and decouples into volumetric and deviatoric parts [20,11]. Although the proposition of local intermediate configuration free from elastic deformations at a given point of the body is physically questionable but the hyperelastic formulation seems to be based on more logical assumptions compared with hypoelastic formulation.

The concept of intermediate configuration has been used by many authors among which Nemat-Nasser [22], Lee and Liu [23], and Simo [20,24] are noteworthy. Simo discussed the importance of intermediate configuration in large deformation elastoplasticity [24]. Based on maximum plastic dissipation and multiplicative decomposition of deformation gradient he provided a formulation for hyperelastic based finite strain plasticity [20,25]. He also presented algorithms that preserve the form of integration scheme in small deformation theory [26]. Perić and de Souza Neto developed a computational model for Tresca plasticity with an optimal parametrization in the space of principal stresses [27]. Eterovic and Bathe formulated a hyperelastic based algorithm using logarithmic stress and strain measures [28]. A review of these and many other works reveals that logarithmic strain measures are favorable due to the simplicity that is induced by the coaxiality of stress and strain.

The development in this work is majorly based on the work of Simo [20,25]. A midpoint rule is applied to the rate form equations governing the evolution of plastic variables and a novel time discrete equation is derived in terms of the variables at midpoint configuration. This approach is in contrast to the usual one in which the backward Euler method is used to connect the variables at final configuration to the ones at the end of previous time step. The consistency condition is enforced at midpoint configuration and then the variables are pushed forward to final configuration. Having calculated the plastic variables, all other variables can be computed by mere function evaluation. Based on the methodology just described, a return mapping algorithm is proposed in which trial variables are obtained by pushing forward the variables at the end of previous time step to midpoint configuration. If they satisfy the consistency condition, they are assumed to be the correct ones otherwise a plastic correction should be applied. The algorithmic setup as well as the detailed derivation of tangent operator consistent with integration scheme is discussed in detail. From the developments, it will be evident that the number of floating point operations required to accomplish a

typical time step is high but the capability of using large time steps without deteriorating the numerical stability leads to a lower computation time. Using benchmark examples, it is shown that the performance of algorithm is remarkable and it has outstanding convergence properties compared with the classical backward Euler method.

The paper is organised as follows. In Section 2, we present the time continuous model based on which the development of algorithm proceeds. In Section 3, the algorithmic setup including the trial and plastic correction steps is described in detail. The linearization of integration algorithm and the derivation of tangent operator is discussed in Section 4. The weak form of the three-field Hu-Washizu functional leading to geometric and material stiffness matrices is presented in Section 5. Benchmark examples are used in Section 6 to investigate the performance and convergence properties of the proposed algorithm. Finally, a few concluding remarks are provided in Section 6.

2. Time continuous model

The time continuous model that is used here is based on the work of Simo. In this section, we only present a brief review of ideas and equations relevant to our work. A detailed discussion of the model and corresponding derivations can be found in [20]. The stress in this model derives from a potential in which the deviatoric and volumetric parts are decoupled. Among all admissible stress states, the one that maximizes the plastic dissipation is the correct stress state. The relative stress should satisfy the yield condition. The flow rule and hardening law govern the evolution of plastic variables and back stress.

In large deformation plasticity, it is usually assumed that at every point of a deformed body there exists an intermediate configuration which is free from elastic deformations. This configuration can be reached from reference configuration using the plastic part, \mathbf{F}^p , of the deformation gradient, \mathbf{F} . The spatial configuration is then obtained from the intermediate stress free configuration by applying the elastic part, \mathbf{F}^e . Based on this assumption, the deformation gradient is expressible as the multiplicative decomposition, $\mathbf{F} = \mathbf{F}^e \mathbf{F}^p$. With the help of this decomposition, the hyperelasticity law for the model can be defined as:

$$W = U(J) + \frac{1}{2}\mu \left(J^{-\frac{2}{3}} \mathbf{b}^e : \mathbf{g} - 3 \right), \quad (1)$$

$$\boldsymbol{\tau} = 2 \frac{\partial W}{\partial \mathbf{g}} = J p \mathbf{g} + \mu J^{-\frac{2}{3}} \text{dev.}(\mathbf{b}^e), \quad (2)$$

$$\boldsymbol{\xi} = \text{dev.}(\boldsymbol{\tau}) - J^{-\frac{2}{3}} \text{dev.}(\mathbf{q}), \quad (3)$$

where W is the free energy, $U(J)$ and the second term in Eq. (1) are, respectively, the volumetric and

deviatoric parts of the free energy, $\mathbf{b}^e = \mathbf{F}^e \mathbf{F}^{eT}$, \mathbf{g} and $\boldsymbol{\tau}$ are the elastic left Cauchy-Green tensor, the metric tensor and the Kirchhoff stress tensor, $p = U'(J)$ is the pressure, and \mathbf{q} and $\boldsymbol{\xi}$ are the back stress and the relative stress tensors. It should, however, be noted that if an orthogonal coordinate system with unit base vectors is adopted, the metric tensor \mathbf{g} reduces to the identity tensor $\mathbf{1}$. Finally μ and J are the rigidity modulus and the determinant of deformation gradient. The yield condition in terms of relative stress has the form:

$$\phi = \|\boldsymbol{\xi}\| - \sqrt{\frac{2}{3}} K(\bar{e}^p) \leq 0, \tag{4}$$

where the function $K'(\bar{e}^p)$ is called the isotropic hardening modulus.

The hypothesis of maximum plastic dissipation leads to the following flow rule governing the evolution of \mathbf{b}^e :

$$\mu J^{-\frac{2}{3}} \text{dev.}(L_v \mathbf{b}^e) = -2\bar{\mu} \dot{\gamma} \mathbf{n}. \tag{5}$$

In this equation, $\dot{\gamma} \geq 0$ is called the plastic consistency parameter or the plastic multiplier, and the parameter $\bar{\mu}$ is defined as:

$$\bar{\mu} = \bar{\mu} - \frac{1}{3} J^{-\frac{2}{3}} \text{tr}(\mathbf{q}), \tag{6}$$

where:

$$\bar{\mu} = \frac{1}{3} \mu J^{-\frac{2}{3}} \text{tr}(\mathbf{b}^e). \tag{7}$$

The tensor \mathbf{n} is the normal to the yield surface and is obtained from:

$$\mathbf{n} = \frac{\boldsymbol{\xi}}{\|\boldsymbol{\xi}\|}. \tag{8}$$

In metal plasticity, it is assumed that plastic deformations are isochoric. Therefore, it is required to impose the condition that $L_v \mathbf{b}^e$ be traceless, i.e.:

$$\text{tr}(L_v \mathbf{b}^e) = 0. \tag{9}$$

A generalization of the approach that is employed in small deformation theory leads to the following kinematic hardening law:

$$J^{-\frac{2}{3}} \text{dev.}(L_v \mathbf{q}) = \frac{2}{3} \frac{\bar{\mu}}{\mu} \dot{\gamma} H'(\bar{e}^p) \mathbf{n}. \tag{10}$$

The term H' appearing in this equation is called the kinematic hardening modulus. Similar to $L_v \mathbf{b}^e$, the traceless condition should be imposed on $L_v \mathbf{q}$ leading to:

$$\text{tr}(L_v \mathbf{q}) = 0. \tag{11}$$

The evolution of equivalent plastic strain, \bar{e}^p , obeys the

simple equation:

$$\dot{\bar{e}}^p = \sqrt{\frac{2}{3}} \dot{\gamma}, \tag{12}$$

which is consistent with the usual definition of plastic strain in small deformation theory.

As a final note on previous equations, it is recalled that $L_v \mathbf{t}$ is the Lie derivative of spatial tensor \mathbf{t} and is defined as:

$$L_v \mathbf{t} = \phi_* \frac{\partial}{\partial t} \phi^* \mathbf{t}, \tag{13}$$

where ϕ_* and ϕ^* are respectively the *push forward* and *pull back* operators. Eqs. (1)-(12) collectively comprise the time continuous model based on which the developments in subsequent sections proceed.

3. Algorithmic setup

In this section, the algorithmic setup is discussed in detail. At first, time discrete equations governing the evolution of \mathbf{b}^e and \mathbf{q} are derived and then the integration scheme comprising of trial, correction and stress updating steps is presented.

3.1. Time discrete model

Starting from Eq. (5) and noting the definition of Lie derivative in Eq. (13) we can write:

$$\begin{aligned} \mu J^{-\frac{2}{3}} \text{dev} \left(\mathbf{F} \frac{\partial}{\partial t} \mathbf{C}^{P-1} \mathbf{F}^T \right) \\ = \mu J^{-\frac{2}{3}} \mathbf{F} \text{DEV} \left(\frac{\partial}{\partial t} \mathbf{C}^{P-1} \right) \mathbf{F}^T = -2\bar{\mu} \dot{\gamma} \mathbf{n}, \end{aligned} \tag{14}$$

where $\mathbf{C}^P = \mathbf{F}^{PT} \mathbf{F}^P$ is the plastic right Cauchy-Green tensor and the deviator of a given tensor \mathbf{T} in reference configuration is computed from the following equation:

$$\text{DEV}(\mathbf{T}) = \mathbf{T} - \frac{1}{3} (\mathbf{T} : \mathbf{C}) \mathbf{C}^{-1}. \tag{15}$$

Pre- and post-multiplication of Eq. (14), respectively by \mathbf{F}^{-1} and \mathbf{F}^{-T} , leads to:

$$\mu J^{-\frac{2}{3}} \text{DEV} \left(\frac{\partial}{\partial t} \mathbf{C}^{P-1} \right) = -2\bar{\mu} \dot{\gamma} \mathbf{F}^{-1} \mathbf{n} \mathbf{F}^{-T} = -2\bar{\mu} \dot{\gamma} \mathbf{N}, \tag{16}$$

where $\mathbf{N} = \phi^*(\mathbf{n})$ is the normal to yield surface in reference configuration.

If we consider a midpoint configuration that can be reached by adding the displacement $\mathbf{u}_{n+\alpha}$ to the body in reference configuration with $\mathbf{u}_{n+\alpha}$ defined as:

$$\mathbf{u}_{n+\alpha} = (1 - \alpha) \mathbf{u}_n + \alpha \mathbf{u}_{n+1}, \quad \alpha \in [0.5, 1], \tag{17}$$

then the deformation gradient from reference configuration to midpoint configuration can be calculated as follows:

$$\mathbf{F}_{n+\alpha} = (1 - \alpha)\mathbf{F}_n + \alpha\mathbf{F}_{n+1}. \tag{18}$$

Since the consistency condition is enforced at midpoint configuration, in subsequent developments frequent reference is made to this configuration.

The application of midpoint rule to Eq. (16) results in the following time discrete equation for the evolution of \mathbf{C}^{P-1} :

$$\begin{aligned} \mu J_{n+\alpha}^{-\frac{2}{3}} \text{DEV}_{n+\alpha} \left(\frac{\mathbf{C}_{n+1}^{P-1} - \mathbf{C}_n^{P-1}}{\Delta t_{n+1}} \right) \\ = -2\bar{\mu}_{n+\alpha} \frac{\Delta \gamma_{n+1}}{\Delta t_{n+1}} \mathbf{N}_{n+\alpha}, \end{aligned} \tag{19}$$

or more conveniently:

$$\begin{aligned} \mu J_{n+\alpha}^{-\frac{2}{3}} \text{DEV}_{n+\alpha} (\mathbf{C}_{n+1}^{P-1}) = \mu J_{n+\alpha}^{-\frac{2}{3}} \text{DEV}_{n+\alpha} (\mathbf{C}_n^{P-1}) \\ - 2\bar{\mu}_{n+\alpha} \Delta \gamma_{n+1} \mathbf{N}_{n+\alpha}. \end{aligned} \tag{20}$$

This equation is the point of departure of our work and the work of Simo [20] in which the backward Euler method is used instead of midpoint rule.

Pushing forward Eq. (20) to midpoint configuration using $\mathbf{F}_{n+\alpha}$ leads to:

$$\begin{aligned} \mu J_{n+\alpha}^{-\frac{2}{3}} \text{dev} (\mathbf{F}_{n+\alpha} \mathbf{C}_{n+1}^{P-1} \mathbf{F}_{n+\alpha}^T) \\ = \mu J_{n+\alpha}^{-\frac{2}{3}} \text{dev} (\mathbf{F}_{n+\alpha} \mathbf{C}_n^{P-1} \mathbf{F}_{n+\alpha}^T) \\ - 2\bar{\mu}_{n+\alpha} \Delta \gamma_{n+1} \mathbf{n}_{n+\alpha}. \end{aligned} \tag{21}$$

We use the convention in [11] for the definition of relative deformation gradients (see Figure 1). According to this convention, $\mathbf{f}_{n+\alpha} = \mathbf{F}_{n+\alpha} \mathbf{F}_n^{-1}$, $\tilde{\mathbf{f}}_{n+\alpha} = \mathbf{F}_{n+1} \mathbf{F}_{n+\alpha}^{-1}$ and $\mathbf{f}_{n+1} = \mathbf{F}_{n+1} \mathbf{F}_n^{-1}$ are, respectively, the relative deformation gradients from configurations \mathbf{x}_n to $\mathbf{x}_{n+\alpha}$, $\mathbf{x}_{n+\alpha}$ to \mathbf{x}_{n+1} and \mathbf{x}_n to \mathbf{x}_{n+1} . Observing that:

$$\begin{aligned} J_{n+\alpha}^{-\frac{2}{3}} (\mathbf{F}_{n+\alpha} \mathbf{C}_{n+1}^{P-1} \mathbf{F}_{n+\alpha}^T) \\ = J_{n+\alpha}^{-\frac{2}{3}} (\mathbf{F}_{n+\alpha} \mathbf{F}_{n+1}^{-1} \mathbf{F}_{n+1} \mathbf{C}_{n+1}^{P-1} \mathbf{F}_{n+1}^T \mathbf{F}_{n+1}^{-T} \mathbf{F}_{n+\alpha}^T) \\ = \left[\left(\frac{J_{n+\alpha}}{J_{n+1}} \right)^{-\frac{1}{3}} \mathbf{F}_{n+\alpha} \mathbf{F}_{n+1}^{-1} \right] \left(J_{n+1}^{-\frac{2}{3}} \mathbf{F}_{n+1} \mathbf{C}_{n+1}^{P-1} \mathbf{F}_{n+1}^T \right) \\ \times \left[\left(\frac{J_{n+\alpha}}{J_{n+1}} \right)^{-\frac{1}{3}} \mathbf{F}_{n+1}^{-T} \mathbf{F}_{n+\alpha}^T \right] = \bar{\mathbf{f}}_{n+\alpha}^{-1} \bar{\mathbf{b}}_{n+1}^e \bar{\mathbf{f}}_{n+\alpha}^{-T}, \end{aligned} \tag{22}$$

and:

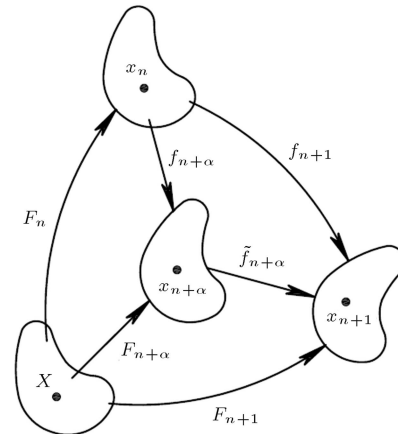


Figure 1. Deformation gradients mapping reference and spatial configurations.

$$\begin{aligned} J_{n+\alpha}^{-\frac{2}{3}} (\mathbf{F}_{n+\alpha} \mathbf{C}_n^{P-1} \mathbf{F}_{n+\alpha}^T) \\ = J_{n+\alpha}^{-\frac{2}{3}} (\mathbf{F}_{n+\alpha} \mathbf{F}_n^{-1} \mathbf{F}_n \mathbf{C}_n^{P-1} \mathbf{F}_n^T \mathbf{F}_n^{-T} \mathbf{F}_{n+\alpha}^T) \\ = \left[\left(\frac{J_{n+\alpha}}{J_n} \right)^{-\frac{1}{3}} \mathbf{F}_{n+\alpha} \mathbf{F}_n^{-1} \right] \left(J_n^{-\frac{2}{3}} \mathbf{F}_n \mathbf{C}_n^{P-1} \mathbf{F}_n^T \right) \\ \times \left[\left(\frac{J_{n+\alpha}}{J_n} \right)^{-\frac{1}{3}} \mathbf{F}_n^{-T} \mathbf{F}_{n+\alpha}^T \right] = \bar{\mathbf{f}}_{n+\alpha} \bar{\mathbf{b}}_n^e \bar{\mathbf{f}}_{n+\alpha}^T. \end{aligned} \tag{23}$$

Eq. (21) can be written in the form:

$$\begin{aligned} \mu \text{dev} \left(\bar{\mathbf{f}}_{n+\alpha}^{-1} \bar{\mathbf{b}}_{n+1}^e \bar{\mathbf{f}}_{n+\alpha}^{-T} \right) = \mu \text{dev} (\bar{\mathbf{f}}_{n+\alpha} \bar{\mathbf{b}}_n^e \bar{\mathbf{f}}_{n+\alpha}^T) \\ - 2\bar{\mu}_{n+\alpha} \Delta \gamma_{n+1} \mathbf{n}_{n+\alpha}. \end{aligned} \tag{24}$$

The tensors appearing in Eqs. (22)-(24) with bars over them are volume preserving tensors. In other words, it is easy to verify that $\text{det}(\bar{\mathbf{t}}) = 1$ for a given tensor $\bar{\mathbf{t}}$.

In the derivation that follows, it is shown that Eq. (24) can be cast into a simpler form. Utilizing Eq. (9) in previous section, we can write:

$$\text{tr} \left(\mathbf{F} \frac{\partial}{\partial t} \mathbf{C}^{P-1} \mathbf{F}^T \right) = 0. \tag{25}$$

Applying midpoint rule, we have:

$$\begin{aligned} \text{tr} \left(\mathbf{F}_{n+\alpha} \frac{\mathbf{C}_{n+1}^{P-1} - \mathbf{C}_n^{P-1}}{\Delta t_{n+1}} \mathbf{F}_{n+\alpha}^T \right) \\ = \frac{1}{\Delta t_{n+1}} [\text{tr}(\mathbf{F}_{n+\alpha} \mathbf{C}_{n+1}^{P-1} \mathbf{F}_{n+\alpha}^T) - \text{tr}(\mathbf{F}_{n+\alpha} \mathbf{C}_n^{P-1} \mathbf{F}_{n+\alpha}^T)] \\ = \frac{1}{\Delta t_{n+1}} [\text{tr}(\mathbf{f}_{n+\alpha}^{-1} \mathbf{b}_{n+1}^e \mathbf{f}_{n+\alpha}^{-T}) - \text{tr}(\mathbf{f}_{n+\alpha} \mathbf{b}_n^e \mathbf{f}_{n+\alpha}^T)] \\ = 0. \end{aligned} \tag{26}$$

Implying that:

$$\text{tr}(\mathbf{f}_{n+\alpha}^{-1} \mathbf{b}_{n+1}^e \mathbf{f}_{n+\alpha}^{-T}) = \text{tr}(\mathbf{f}_{n+\alpha} \mathbf{b}_n^e \mathbf{f}_{n+\alpha}^T). \quad (27)$$

Therefore, Eq. (24) transforms to:

$$\bar{\mathbf{f}}_{n+\alpha}^{-1} \bar{\mathbf{b}}_{n+1}^e \bar{\mathbf{f}}_{n+\alpha}^{-T} = \bar{\mathbf{f}}_{n+\alpha} \bar{\mathbf{b}}_n^e \bar{\mathbf{f}}_{n+\alpha}^T - 2 \frac{\bar{\mu}_{n+\alpha}}{\mu} \Delta\gamma_{n+1} \mathbf{n}_{n+\alpha}. \quad (28)$$

Eq. (28) has an interesting geometrical interpretation. According to this equation, the tensor \mathbf{b}^e at final configuration (time instant t_{n+1}) pulled back to midpoint configuration is equal to push forward to midpoint configuration of \mathbf{b}^e at the end of previous time step (time instant t_n) minus the plastic correction at midpoint configuration (second term on the right hand side). Another useful equation that is needed in our subsequent developments is obtained by pushing forward Eq. (28) to final configuration using $\bar{\mathbf{f}}_{n+\alpha}$. This leads to:

$$\bar{\mathbf{b}}_{n+1}^e = \bar{\mathbf{f}}_{n+1} \bar{\mathbf{b}}_n^e \bar{\mathbf{f}}_{n+1}^T - 2 \frac{\bar{\mu}_{n+\alpha}}{\mu} \Delta\gamma_{n+1} \bar{\mathbf{f}}_{n+1} \mathbf{n}_{n+\alpha} \bar{\mathbf{f}}_{n+1}^T. \quad (29)$$

Thus, at the end of each time step, the tensor \mathbf{b}^e , instead of its deviator, can be saved directly.

It is easy to show that similar computations using Eqs. (10) and (11), as starting point, result in the following set of equations governing the evolution of \mathbf{q} :

$$\begin{aligned} \text{dev}\left(\bar{\mathbf{f}}_{n+\alpha}^{-1} \bar{\mathbf{q}}_{n+1} \bar{\mathbf{f}}_{n+\alpha}^{-T}\right) &= \text{dev}\left(\bar{\mathbf{f}}_{n+\alpha} \bar{\mathbf{q}}_n \bar{\mathbf{f}}_{n+\alpha}^T\right) \\ &+ \sqrt{\frac{2}{3}} \frac{\bar{\mu}_{n+\alpha}}{\mu} \Delta H_{n+1} \mathbf{n}_{n+\alpha}, \end{aligned} \quad (30)$$

$$\begin{aligned} \bar{\mathbf{f}}_{n+\alpha}^{-1} \bar{\mathbf{q}}_{n+1} \bar{\mathbf{f}}_{n+\alpha}^{-T} &= \bar{\mathbf{f}}_{n+\alpha} \bar{\mathbf{q}}_n \bar{\mathbf{f}}_{n+\alpha}^T \\ &+ \sqrt{\frac{2}{3}} \frac{\bar{\mu}_{n+\alpha}}{\mu} \Delta H_{n+1} \mathbf{n}_{n+\alpha}, \end{aligned} \quad (31)$$

$$\begin{aligned} \bar{\mathbf{q}}_{n+1} &= \bar{\mathbf{f}}_{n+1} \bar{\mathbf{q}}_n \bar{\mathbf{f}}_{n+1}^T \\ &+ \sqrt{\frac{2}{3}} \frac{\bar{\mu}_{n+\alpha}}{\mu} \Delta H_{n+1} \bar{\mathbf{f}}_{n+1} \mathbf{n}_{n+\alpha} \bar{\mathbf{f}}_{n+1}^T, \end{aligned} \quad (32)$$

where:

$$\Delta H_{n+1} = H(\bar{e}_{n+1}^p) - H(\bar{e}_n^p). \quad (33)$$

The evolution of internal variable, \bar{e}^p , follows from the application of midpoint rule to Eq. (12) leading to:

$$\bar{e}_{n+1}^p = \bar{e}_n^p + \sqrt{\frac{2}{3}} \Delta\gamma_{n+1}. \quad (34)$$

3.2. Trial step

The evolution of \mathbf{b}^e and \mathbf{q} in trial step is assumed to be elastic. Based on this assumption, the equations that identify the trial step at midpoint configuration can be obtained by setting the incremental plastic multiplier $\Delta\gamma_{n+1}$ to zero in Eqs. (28), (31) and (34). Therefore, we have:

$$\bar{\mathbf{b}}_{n+\alpha}^{e,\text{trial}} = \bar{\mathbf{f}}_{n+\alpha} \bar{\mathbf{b}}_n^e \bar{\mathbf{f}}_{n+\alpha}^T, \quad (35)$$

$$\boldsymbol{\tau}_{n+\alpha}^{\text{trial}} = J_{n+\alpha} p_{n+\alpha} \mathbf{g} + \mu \text{dev}(\bar{\mathbf{b}}_{n+\alpha}^{e,\text{trial}}), \quad (36)$$

$$\bar{\mathbf{q}}_{n+\alpha}^{\text{trial}} = \bar{\mathbf{f}}_{n+\alpha} \bar{\mathbf{q}}_n \bar{\mathbf{f}}_{n+\alpha}^T, \quad (37)$$

$$\begin{aligned} \boldsymbol{\xi}_{n+\alpha}^{\text{trial}} &= \text{dev}(\boldsymbol{\tau}_{n+\alpha}^{\text{trial}}) - \text{dev}(\bar{\mathbf{q}}_{n+\alpha}^{\text{trial}}) \\ &= \text{dev}(\mu \bar{\mathbf{b}}_{n+\alpha}^{e,\text{trial}} - \bar{\mathbf{q}}_{n+\alpha}^{\text{trial}}), \end{aligned} \quad (38)$$

$$\bar{e}_{n+1}^{p,\text{trial}} = \bar{e}_n^p. \quad (39)$$

If the trial relative stress satisfies the yield condition, i.e. if:

$$\|\boldsymbol{\xi}_{n+\alpha}^{\text{trial}}\| - \sqrt{\frac{2}{3}} K(\bar{e}_{n+\alpha}^{p,\text{trial}}) \leq 0, \quad (40)$$

the elastic assumption is correct and the final stress state can be computed by pushing forward $\bar{\mathbf{b}}_{n+\alpha}^{e,\text{trial}}$ and $\bar{\mathbf{q}}_{n+\alpha}^{\text{trial}}$ to final configuration (see Section 3.4).

3.3. Correction step

If the condition in Eq. (40) is not satisfied, a plastic correction should be applied. In this case, the incremental plastic multiplier $\Delta\gamma_{n+1}$ is not zero and speculation of Eqs. (28), (31) and (34) with regard to Eqs. (35)-(39) results in the following set of equations:

$$\bar{\mathbf{b}}_{n+\alpha}^e = \bar{\mathbf{b}}_{n+\alpha}^{e,\text{trial}} - 2 \frac{\bar{\mu}_{n+\alpha}}{\mu} \Delta\gamma_{n+1} \mathbf{n}_{n+\alpha}, \quad (41)$$

$$\boldsymbol{\tau}_{n+\alpha} = J_{n+\alpha} p_{n+\alpha} \mathbf{g} + \mu \text{dev}(\bar{\mathbf{b}}_{n+\alpha}^e), \quad (42)$$

$$\bar{\mathbf{q}}_{n+\alpha} = \bar{\mathbf{q}}_{n+\alpha}^{\text{trial}} + \sqrt{\frac{2}{3}} \frac{\bar{\mu}_{n+\alpha}}{\mu} \Delta H_{n+1} \mathbf{n}_{n+\alpha}, \quad (43)$$

$$\begin{aligned} \boldsymbol{\xi}_{n+\alpha} &= \text{dev}(\boldsymbol{\tau}_{n+\alpha}) - \text{dev}(\bar{\mathbf{q}}_{n+\alpha}) \\ &= \boldsymbol{\xi}_{n+\alpha}^{\text{trial}} - 2 \bar{\mu}_{n+\alpha} \left(1 + \frac{H'_{n+\alpha}}{3\mu}\right) \Delta\gamma_{n+1} \mathbf{n}_{n+\alpha}, \end{aligned} \quad (44)$$

$$\bar{e}_{n+1}^p = \bar{e}_{n+1}^{p,\text{trial}} + \alpha \sqrt{\frac{2}{3}} \Delta\gamma_{n+1}. \quad (45)$$

Eq. (44) together with Eq. (8) in Section 2 implies that $\boldsymbol{\xi}_{n+\alpha}$ and $\boldsymbol{\xi}_{n+\alpha}^{\text{trial}}$ are coaxial and we have the following relations:

$$\mathbf{n}_{n+\alpha} = \frac{\boldsymbol{\xi}_{n+\alpha}}{\|\boldsymbol{\xi}_{n+\alpha}\|} = \frac{\boldsymbol{\xi}_{n+\alpha}^{\text{trial}}}{\|\boldsymbol{\xi}_{n+\alpha}^{\text{trial}}\|}, \quad (46)$$

$$\|\boldsymbol{\xi}_{n+\alpha}\| = \|\boldsymbol{\xi}_{n+\alpha}^{\text{trial}}\| - 2\bar{\mu}_{n+\alpha} \left(1 + \frac{H'_{n+\alpha}}{3\mu}\right) \Delta\gamma_{n+1}. \quad (47)$$

The term $\Delta\gamma_{n+1}$ appearing in previous equations can be computed by enforcing the consistency condition at midpoint configuration. In other words, the following condition should be satisfied:

$$\begin{aligned} \phi(\bar{e}_{n+\alpha}^p) &= \|\boldsymbol{\xi}_{n+\alpha}\| - \sqrt{\frac{2}{3}}K(\bar{e}_{n+\alpha}^p) \\ &= \|\boldsymbol{\xi}_{n+\alpha}^{\text{trial}}\| - 2\bar{\mu}_{n+\alpha} \left(1 + \frac{H'_{n+\alpha}}{3\mu}\right) \Delta\gamma_{n+1} \\ &\quad - \sqrt{\frac{2}{3}}K(\bar{e}_{n+\alpha}^p) = 0. \end{aligned} \quad (48)$$

This equation can be nonlinear depending on the choice of $K(\bar{e}^p)$ and $H(\bar{e}^p)$, and thus should be solved iteratively for $\Delta\gamma_{n+1}$. Substituting the result into Eqs. (41)-(45) completely defines the stress state at midpoint configuration.

3.4. Stress updating step

Although the consistency condition is enforced at midpoint configuration, it is however desired to have the stress state in final configuration. For this purpose, $\bar{\mathbf{b}}_{n+\alpha}^e$ and $\bar{\mathbf{q}}_{n+\alpha}$ from Section 3.2 or 3.3, whichever applicable, are pushed forward to final configuration using $\bar{\mathbf{f}}_{n+\alpha}$. The Kirchhoff stress tensor can then be computed by direct function evaluation. The following equations summarize the procedure needed to update the stress state in final configuration:

$$\bar{\mathbf{b}}_{n+1}^e = \bar{\mathbf{f}}_{n+\alpha} \bar{\mathbf{b}}_{n+\alpha}^e \bar{\mathbf{f}}_{n+\alpha}^T, \quad (49)$$

$$\boldsymbol{\tau}_{n+1} = J_{n+1} p_{n+1} \mathbf{g} + \mu \text{dev}(\bar{\mathbf{b}}_{n+1}^e), \quad (50)$$

$$\bar{\mathbf{q}}_{n+1} = \bar{\mathbf{f}}_{n+\alpha} \bar{\mathbf{q}}_{n+\alpha} \bar{\mathbf{f}}_{n+\alpha}^T, \quad (51)$$

$$\boldsymbol{\xi}_{n+1} = \text{dev}(\boldsymbol{\tau}_{n+1}) - \text{dev}(\bar{\mathbf{q}}_{n+1}). \quad (52)$$

Moreover, computing the internal variable, \bar{e}_{n+1}^p , with the help of Eq. (34) completes the updating procedure.

It is important to emphasize that \mathbf{b}^e and \mathbf{q} are the driving parameters of the algorithm proposed above and the hyperelastic nature of this algorithm is preserved at all configurations. In other words, having calculated \mathbf{b}^e at a given configuration, the Kirchhoff stress tensor can be computed from the associated potential W at that configuration (see Eqs. (1) and (2)).

4. Consistent tangent operator

The tangent operator consistent with the algorithm described in preceding sections is developed in this

section. The linearization of algorithm is discussed in detail and some issues concerning the derivative of right Cauchy-Green tensor is presented next.

4.1. Linearization

Eq. (50) combined with Eq. (29) can be written in the following form:

$$\boldsymbol{\tau}_{n+1} = \boldsymbol{\tau}_{n+1}^{\text{vol}} + \boldsymbol{\tau}_{n+1}^{\text{dev, tr}} - \boldsymbol{\tau}_{n+1}^{\text{dev, cr}}, \quad (53)$$

where $\boldsymbol{\tau}_{n+1}^{\text{vol}}$ is the volumetric part of the stress and $\boldsymbol{\tau}_{n+1}^{\text{dev, tr}}$ and $\boldsymbol{\tau}_{n+1}^{\text{dev, cr}}$ are, respectively, the trial and corrected parts of the deviatoric stress. The definition of individual terms is presented below:

$$\boldsymbol{\tau}_{n+1}^{\text{vol}} = J_{n+1} p_{n+1} \mathbf{g}, \quad (54)$$

$$\boldsymbol{\tau}_{n+1}^{\text{dev, tr}} = \mu \text{dev}(\bar{\mathbf{f}}_{n+1} \bar{\mathbf{b}}_n^e \bar{\mathbf{f}}_{n+1}^T), \quad (55)$$

$$\boldsymbol{\tau}_{n+1}^{\text{dev, cr}} = 2\bar{\mu}_{n+\alpha} \Delta\gamma_{n+1} \text{dev}(\bar{\mathbf{f}}_{n+\alpha} \mathbf{n}_{n+\alpha} \bar{\mathbf{f}}_{n+\alpha}^T). \quad (56)$$

The tangent operator at time instant, t_{n+1} , is defined as:

$$\mathbf{a}_{n+1} = 2 \frac{\partial \boldsymbol{\tau}_{n+1}}{\partial \mathbf{g}} = \mathbf{a}_{n+1}^{\text{vol}} + \mathbf{a}_{n+1}^{\text{dev, tr}} - \mathbf{a}_{n+1}^{\text{dev, cr}}. \quad (57)$$

It is easy to show that [20,25]:

$$\begin{aligned} \mathbf{a}_{n+1}^{\text{vol}} &= 2 \frac{\partial \boldsymbol{\tau}_{n+1}^{\text{vol}}}{\partial \mathbf{g}} = J_{n+1}^2 U''(J_{n+1}) \mathbf{g} \otimes \mathbf{g} \\ &\quad + J_{n+1} p_{n+1} (\mathbf{g} \otimes \mathbf{g} - 2\mathbf{I}), \end{aligned} \quad (58)$$

and:

$$\begin{aligned} \mathbf{a}_{n+1}^{\text{dev, tr}} &= 2 \frac{\partial \boldsymbol{\tau}_{n+1}^{\text{dev, tr}}}{\partial \mathbf{g}} = 2\bar{\mu} \left(\mathbf{I} - \frac{1}{3} \mathbf{g} \otimes \mathbf{g} \right) \\ &\quad - \frac{2}{3} \left(\boldsymbol{\tau}_{n+1}^{\text{dev, tr}} \otimes \mathbf{g} + \mathbf{g} \otimes \boldsymbol{\tau}_{n+1}^{\text{dev, tr}} \right), \end{aligned} \quad (59)$$

where \mathbf{I} is the fourth order identity tensor.

In order to facilitate the derivation of $\mathbf{a}_{n+1}^{\text{dev, cr}}$, we define the following auxiliary term:

$$\mathbf{n}_{n+1}^* = \text{dev} \left(\bar{\mathbf{f}}_{n+\alpha} \mathbf{n}_{n+\alpha} \bar{\mathbf{f}}_{n+\alpha}^T \right). \quad (60)$$

Additionally we define:

$$\boldsymbol{\Gamma}_n = \phi^*(\mathbf{q}_n), \quad (61)$$

$$\mathbf{E}_n = \mu \mathbf{C}_n^{P-1} - \boldsymbol{\Gamma}_n, \quad (62)$$

$$\mathbf{T}_{n+\alpha} = \text{DEV}_{n+\alpha}(\mathbf{E}_n), \quad (63)$$

$$\boldsymbol{\Xi}_{n+1} = J_{n+1}^{-\frac{2}{3}} \text{DEV}_{n+1}(\mathbf{T}_{n+\alpha}). \quad (64)$$

With the help of the aforementioned terms, Eq. (56), pulled back to reference configuration, is expressed as:

$$\mathbf{S}_{n+1}^{\text{dev,cr}} = 2\bar{\mu}_{n+\alpha} \Delta\gamma_{n+1} \mathbf{N}_{n+1}^*, \quad (65)$$

where:

$$\mathbf{N}_{n+1}^* = \phi^*(\mathbf{n}_{n+1}^*) = \frac{1}{\|\boldsymbol{\xi}_{n+\alpha}^{\text{trial}}\|} \boldsymbol{\Xi}_{n+1}. \quad (66)$$

For the tangent operator in reference configuration we can write:

$$\begin{aligned} \mathbf{C}_{n+1}^{\text{dev,cr}} = & 2 \frac{\partial \mathbf{S}_{n+1}^{\text{dev,cr}}}{\partial \mathbf{C}_{n+1}} = 4\Delta\gamma_{n+1} \mathbf{N}_{n+1}^* \otimes \frac{\partial \bar{\mu}_{n+\alpha}}{\partial \mathbf{C}_{n+1}} \\ & + 4\bar{\mu}_{n+\alpha} \mathbf{N}_{n+1}^* \otimes \frac{\partial \Delta\gamma_{n+1}}{\partial \mathbf{C}_{n+1}} \\ & + 4\bar{\mu}_{n+\alpha} \Delta\gamma_{n+1} \frac{\partial \mathbf{N}_{n+1}^*}{\partial \mathbf{C}_{n+1}}. \end{aligned} \quad (67)$$

The derivative of $\bar{\mu}_{n+\alpha}$ with respect to \mathbf{C}_{n+1} is calculated using its definition in Eq. (6). The result of this calculation can be cast into the following form:

$$\frac{\partial \bar{\mu}_{n+\alpha}}{\partial \mathbf{C}_{n+1}} = \frac{1}{3} \|\boldsymbol{\xi}_{n+\alpha}^{\text{trial}}\| \mathbf{N}_{n+\alpha} : \mathbf{A}_{n+1}, \quad (68)$$

where:

$$\mathbf{N}_{n+\alpha} = \phi^*(\mathbf{n}_{n+\alpha}) = \frac{J_{n+\alpha}^{-\frac{2}{3}}}{\|\boldsymbol{\xi}_{n+\alpha}^{\text{trial}}\|} \mathbf{T}_{n+\alpha}, \quad (69)$$

and:

$$\mathbf{A}_{n+1} = \frac{\partial \mathbf{C}_{n+\alpha}}{\partial \mathbf{C}_{n+1}}, \quad (70)$$

is the change in $\mathbf{C}_{n+\alpha}$ relative to \mathbf{C}_{n+1} (see Section 4.2). The derivative of $\Delta\gamma_{n+1}$ with respect to \mathbf{C}_{n+1} is computed using Eq. (48). We have:

$$\begin{aligned} \frac{\partial \Delta\gamma_{n+1}}{\partial \mathbf{C}_{n+1}} = & \frac{1}{\delta_0} \\ & \left[\frac{\partial \|\boldsymbol{\xi}_{n+\alpha}^{\text{trial}}\|}{\partial \mathbf{C}_{n+\alpha}} - 2\Delta\gamma_{n+1} \left(1 + \frac{H'_{n+\alpha}}{3\mu} \right) \frac{\partial \bar{\mu}_{n+\alpha}}{\partial \mathbf{C}_{n+\alpha}} \right] \\ & : \mathbf{A}_{n+1}, \end{aligned} \quad (71)$$

where:

$$\delta_0 = 2\bar{\mu}_{n+\alpha} \left(1 + \frac{H'_{n+\alpha}}{3\mu} + \alpha \frac{K'_{n+\alpha}}{3\bar{\mu}_{n+\alpha}} \right). \quad (72)$$

With the help of Eq. (38):

$$\begin{aligned} \frac{\partial \|\boldsymbol{\xi}_{n+\alpha}^{\text{trial}}\|}{\partial \mathbf{C}_{n+1}} = & \left[\bar{\mu}_{n+\alpha} \mathbf{N}_{n+\alpha} + \|\boldsymbol{\xi}_{n+\alpha}^{\text{trial}}\| \text{DEV}_{n+\alpha} \right. \\ & \left. (\mathbf{N}_{n+\alpha} \mathbf{C}_{n+\alpha} \mathbf{N}_{n+\alpha}^T) \right] : \mathbf{A}_{n+1}. \end{aligned} \quad (73)$$

Eq. (66) can be used to compute the derivative of \mathbf{N}_{n+1}^* with respect to \mathbf{C}_{n+1} . This computation leads to:

$$\frac{\partial \mathbf{N}_{n+1}^*}{\partial \mathbf{C}_{n+1}} = \frac{1}{\|\boldsymbol{\xi}_{n+\alpha}^{\text{trial}}\|} \left(\frac{\partial \boldsymbol{\Xi}_{n+1}}{\partial \mathbf{C}_{n+1}} - \mathbf{N}_{n+1}^* \otimes \frac{\partial \|\boldsymbol{\xi}_{n+\alpha}^{\text{trial}}\|}{\partial \mathbf{C}_{n+1}} \right). \quad (74)$$

Observing Eq. (64), the following expression is obtained for the derivative of $\boldsymbol{\Xi}_{n+1}$ with respect to \mathbf{C}_{n+1} :

$$\begin{aligned} \frac{\partial \boldsymbol{\Xi}_{n+1}}{\partial \mathbf{C}_{n+1}} = & \frac{1}{3} J_{n+1}^{-\frac{2}{3}} (\mathbf{T}_{n+\alpha} : \mathbf{C}_{n+1}) \\ & \left(\mathbf{I}_{n+1}^C - \frac{1}{3} \mathbf{C}_{n+1}^{-1} \otimes \mathbf{C}_{n+1}^{-1} \right) \\ & - \frac{1}{3} (\boldsymbol{\Xi}_{n+1} \otimes \mathbf{C}_{n+1}^{-1} + \mathbf{C}_{n+1}^{-1} \otimes \boldsymbol{\Xi}_{n+1}) \\ & + J_{n+1}^{-\frac{2}{3}} \text{DEV}_{n+1} \left(\frac{\partial \mathbf{T}_{n+\alpha}}{\partial \mathbf{C}_{n+\alpha}} \right) : \mathbf{A}_{n+1}. \end{aligned} \quad (75)$$

In this equation, \mathbf{I}^C is a fourth order tensor in reference configuration with the following components:

$$I_{IJKL}^C = \frac{1}{2} (C_{IK}^{-1} C_{JL}^{-1} + C_{IL}^{-1} C_{JK}^{-1}). \quad (76)$$

The derivative of $\mathbf{T}_{n+\alpha}$ with respect to \mathbf{C}_{n+1} can be computed using Eq. (63) together with Eq. (62). The final expression has the form:

$$\begin{aligned} \frac{\partial \mathbf{T}_{n+\alpha}}{\partial \mathbf{C}_{n+\alpha}} = & \frac{1}{3} \left[(\mathbf{E}_n : \mathbf{C}_{n+\alpha}) \left(\mathbf{I}_{n+\alpha}^C - \frac{1}{3} \mathbf{C}_{n+\alpha}^{-1} \otimes \mathbf{C}_{n+\alpha}^{-1} \right) \right. \\ & \left. - \mathbf{C}_{n+\alpha}^{-1} \otimes \mathbf{T}_{n+\alpha} \right], \end{aligned} \quad (77)$$

and its deviator with respect to the metric \mathbf{C}_{n+1} in reference configuration is:

$$\begin{aligned} \text{DEV}_{n+1} \left(\frac{\partial \mathbf{T}_{n+\alpha}}{\partial \mathbf{C}_{n+\alpha}} \right) = & \frac{\partial \mathbf{T}_{n+\alpha}}{\partial \mathbf{C}_{n+\alpha}} - \frac{1}{3} \mathbf{C}_{n+1}^{-1} \\ & \otimes \left(\mathbf{C}_{n+1} : \frac{\partial \mathbf{T}_{n+\alpha}}{\partial \mathbf{C}_{n+\alpha}} \right). \end{aligned} \quad (78)$$

Substituting Eqs. (68), (71) and (74) into Eq. (67) and pushing forward to spatial configuration leads to:

$$\begin{aligned} \mathbf{a}_{n+1}^{\text{dev,cr}} = & \frac{4}{3} \bar{\mu}_{n+\alpha} \Delta\gamma_{n+1} \left[\text{tr}(\mathbf{n}_{n+1}) (\mathbf{I} - \frac{1}{3} \mathbf{g} \otimes \mathbf{g}) \right. \\ & \left. - (\mathbf{n}_{n+1}^* \otimes \mathbf{g} + \mathbf{g} \otimes \mathbf{n}_{n+1}^*) \right] \\ & + \phi_* \left\{ \left[2J_{n+1}^{-\frac{2}{3}} f_0 \text{DEV}_{n+1} \left(\frac{\partial \mathbf{T}_{n+\alpha}}{\partial \mathbf{C}_{n+\alpha}} \right) \right] \right\} \end{aligned}$$

$$\begin{aligned}
 & + \delta_1 \mathbf{N}_{n+1}^* \otimes \mathbf{N}_{n+\alpha} + \delta_2 \mathbf{N}_{n+1}^* \\
 & \otimes \text{DEV}_{n+\alpha} (\mathbf{N}_{n+\alpha} \mathbf{C}_{n+\alpha} \mathbf{N}_{n+\alpha}^T) \\
 & : \mathbf{A}_{n+1} \left. \vphantom{\mathbf{A}_{n+1}} \right\}^{\text{sym}}, \tag{79}
 \end{aligned}$$

where:

$$\mathbf{n}_{n+1} = \bar{\mathbf{f}}_{n+\alpha} \mathbf{n}_{n+\alpha} \bar{\mathbf{f}}_{n+\alpha}^T, \tag{80}$$

$$f_0 = \frac{2\bar{\mu}_{n+\alpha} \Delta \gamma_{n+1}}{\|\boldsymbol{\xi}_{n+\alpha}^{\text{trial}}\|}, \tag{81}$$

$$\begin{aligned}
 \delta_1 & = 2\bar{\mu}_{n+\alpha} f_1 - \frac{4}{3} \Delta \gamma_{n+1} \|\boldsymbol{\xi}_{n+\alpha}^{\text{trial}}\| \\
 & \left[\frac{1}{\delta_0} \left(1 + \frac{H'_{n+\alpha}}{3\mu} \right) - 1 \right], \tag{82}
 \end{aligned}$$

$$\delta_2 = 2\|\boldsymbol{\xi}_{n+\alpha}^{\text{trial}}\| f_1, \tag{83}$$

with:

$$f_1 = \frac{1}{\delta_0} - f_0. \tag{84}$$

4.2. Relative metric derivative

In order to finalize the derivation of consistent tangent operator, it is required to compute the change in $\mathbf{C}_{n+\alpha}$ relative to \mathbf{C}_{n+1} . The deformation gradient from reference configuration to midpoint configuration, $\mathbf{F}_{n+\alpha}$, is expressed in terms of \mathbf{F}_n and \mathbf{F}_{n+1} according to Eq. (18). With the help of this equation, the following expression is obtained for $\mathbf{C}_{n+\alpha}$:

$$\begin{aligned}
 \mathbf{C}_{n+\alpha} & = (1-\alpha)^2 \mathbf{C}_n + \alpha(1-\alpha) \mathbf{F}_n^T \mathbf{F}_{n+1} \\
 & + \alpha(1-\alpha) \mathbf{F}_{n+1}^T \mathbf{F}_n + \alpha^2 \mathbf{C}_{n+1}. \tag{85}
 \end{aligned}$$

Using the polar decomposition, $\mathbf{F}_{n+1} = \mathbf{R}_{n+1} \mathbf{U}_{n+1}$, the previous equation transforms to:

$$\begin{aligned}
 \mathbf{C}_{n+\alpha} & = (1-\alpha)^2 \mathbf{C}_n + \alpha^2 \mathbf{C}_{n+1} + \alpha(1-\alpha) [\mathbf{Q}_{n+1} \mathbf{U}_{n+1} \\
 & + \mathbf{U}_{n+1} \mathbf{Q}_{n+1}^T], \tag{86}
 \end{aligned}$$

where:

$$\mathbf{Q}_{n+1} = \mathbf{F}_n^T \mathbf{R}_{n+1}. \tag{87}$$

The derivative of $\mathbf{C}_{n+\alpha}$ with respect to \mathbf{C}_{n+1} can be expressed in component form as:

$$(\mathbf{A}_{n+1})_{IJKL} = \frac{\partial (\mathbf{C}_{n+\alpha})_{IJ}}{\partial (\mathbf{C}_{n+1})_{KL}} = \alpha^2 I_{IJKL}$$

$$\begin{aligned}
 & + \alpha(1-\alpha) \left[(\mathbf{Q}_{n+1})_{IM} \frac{\partial (\mathbf{U}_{n+1})_{MJ}}{\partial (\mathbf{C}_{n+1})_{KL}} \right. \\
 & \left. + \frac{\partial (\mathbf{U}_{n+1})_{IM}}{\partial (\mathbf{C}_{n+1})_{KL}} (\mathbf{Q}_{n+1})_{JM} \right]. \tag{88}
 \end{aligned}$$

It should be noted that in this formulation an equation was provided for the evolution of $\mathbf{b}^e = \mathbf{F}^e \mathbf{F}^{eT}$, which is a symmetric tensor, and not for \mathbf{F}^e itself. Therefore, the intermediate configuration is determined up to an arbitrary rigid body rotation. In other words, considering another intermediate configuration with $\mathbf{F}^{e*} = \mathbf{F}^e \mathbf{Q}^{*T}$ and $\mathbf{F}^{p*} = \mathbf{Q}^* \mathbf{F}^p$ that is obtained from the first by applying the rigid body rotation \mathbf{Q}^* such that $\mathbf{F}^{e*} \mathbf{F}^{p*} = \mathbf{F}^e \mathbf{F}^p = \mathbf{F}$ leads to the same results [11,20,29-31]. Moreover, no rate equation was provided for the evolution of rotation, since it was assumed that the response of material is isotropic in plastic limit (see [32,29] for more information). Therefore, the derivative of \mathbf{R}_{n+1} cannot be determined with respect to \mathbf{C}_{n+1} .

The derivative of \mathbf{U}_{n+1} with respect to \mathbf{C}_{n+1} is computed by noting that $\mathbf{U} = \sqrt{\mathbf{C}}$. Thus we can write:

$$\mathbf{U} = \sqrt{\lambda_1} \mathbf{E}_1 + \sqrt{\lambda_2} \mathbf{E}_2 + \sqrt{\lambda_3} \mathbf{E}_3, \tag{89}$$

where λ_1, λ_2 and λ_3 are distinct eigenvalues of \mathbf{C} , and $\mathbf{E}_1, \mathbf{E}_2$ and \mathbf{E}_3 are the corresponding eigenprojections. For an axisymmetric problem, $\mathbf{E}_3 = \mathbf{e}_3 \otimes \mathbf{e}_3$ and therefore we have [33]:

$$\begin{aligned}
 \frac{\partial \mathbf{E}_i}{\partial \mathbf{C}} & = \frac{1}{\lambda_i - \lambda_j} (\mathbf{I} - \mathbf{E}_i \otimes \mathbf{E}_i - \mathbf{E}_j \otimes \mathbf{E}_j), \\
 & \text{for } i \neq j \text{ and } i, j \in \{1, 2\}, \tag{90}
 \end{aligned}$$

$$\frac{\partial \mathbf{E}_3}{\partial \mathbf{C}} = \mathbf{0}, \tag{91}$$

and:

$$\frac{\partial \sqrt{\lambda_i}}{\partial \mathbf{C}} = \frac{1}{2\sqrt{\lambda_i}} \mathbf{E}_i, \quad i, j \in \{1, 2, 3\}. \tag{92}$$

If $\lambda_1 = \lambda_2 = \lambda$, Eqs. (89), (90) and (92) reduce to the followings:

$$\mathbf{U} = \sqrt{\lambda} \mathbf{E} + \sqrt{\lambda_3} \mathbf{E}_3, \tag{93}$$

$$\frac{\partial \mathbf{E}}{\partial \mathbf{C}} = \frac{1}{\lambda} (\mathbf{I} - \frac{1}{2} \mathbf{E} \otimes \mathbf{E}), \tag{94}$$

and:

$$\frac{\partial \sqrt{\lambda}}{\partial \mathbf{C}} = \frac{1}{4\sqrt{\lambda}} \mathbf{E}. \tag{95}$$

Observing Eqs. (89)-(95), we can write:

$$\begin{aligned} \frac{\partial \mathbf{U}}{\partial \mathbf{C}} = & \frac{1}{\sqrt{\lambda_1} + \sqrt{\lambda_2}} \left[\mathbf{I} + \frac{1}{2} \left(\sqrt{\frac{\lambda_2}{\lambda_1}} - 1 \right) \mathbf{E}_1 \otimes \mathbf{E}_1 \right. \\ & \left. + \frac{1}{2} \left(\sqrt{\frac{\lambda_1}{\lambda_2}} - 1 \right) \mathbf{E}_2 \otimes \mathbf{E}_2 \right] \\ & + \frac{1}{2\sqrt{\lambda_3}} \mathbf{E}_3 \otimes \mathbf{E}_3, \end{aligned} \quad (96)$$

for distinct eigenvalues and:

$$\frac{\partial \mathbf{U}}{\partial \mathbf{C}} = \frac{1}{\sqrt{\lambda}} \left(\mathbf{I} - \frac{1}{4} \mathbf{E} \otimes \mathbf{E} \right) + \frac{1}{2\sqrt{\lambda_3}} \mathbf{E}_3 \otimes \mathbf{E}_3 \quad (97)$$

for $\lambda_1 = \lambda_2 = \lambda$.

5. Variational formulation

In this section, the variational formulation of the elastoplastic boundary value problem using the finite element method is presented. Considering that the formulation is discussed with great details in [20,34], we only present the final results relevant to our work.

5.1. Hu-Washizu variational principle

In Section 2, it was stated that the potential in the time continuous model described in that section is decoupled into volumetric and deviator parts. Hence, defining $\bar{\mathbf{F}} = J^{-\frac{1}{3}} \mathbf{F}$ and $\bar{\mathbf{C}} = \bar{\mathbf{F}}^T \bar{\mathbf{F}}$, the functional, considered in this work, is as follows:

$$\begin{aligned} \Pi(\varphi, \theta, p) = & \int_{\Omega} [U(\theta) + \bar{W}(\bar{\mathbf{C}}, \mathbf{C}^P) + p(J - \theta)] \\ & d\Omega - \Pi_{\text{ext}}(\varphi), \end{aligned} \quad (98)$$

with:

$$\Pi_{\text{ext}}(\varphi) = \int_{\Omega} \mathbf{B} \cdot \varphi d\Omega + \int_{\partial_{\tau}\Omega} \bar{\mathbf{t}} \cdot \varphi d\Gamma, \quad (99)$$

where φ maps every point in reference configuration, Ω , to corresponding point in spatial configuration, $\varphi(\Omega)$, θ is the dilatation, p is the pressure, \mathbf{B} is the body force and $\bar{\mathbf{t}}$ is the prescribed traction on the boundary $\partial_{\tau}\Omega$. In Eq. (98), the purpose of the last term under the integral sign is to enforce the constraint $J = \theta$ and, therefore, the pressure p is the Lagrange multiplier.

Considering an admissible variation $\boldsymbol{\eta}$ in φ , the derivative of Π in the direction $\boldsymbol{\eta}$ leads to the following equation:

$$G = D\Pi \cdot \boldsymbol{\eta} = \int_{\Omega} \boldsymbol{\tau} : (\nabla \boldsymbol{\eta}) d\Omega - G_{\text{ext}} = 0, \quad (100)$$

where:

$$\boldsymbol{\tau} = pJ\mathbf{1} + 2\text{dev} \left(\bar{\mathbf{F}} \frac{\partial \bar{W}}{\partial \bar{\mathbf{C}}} \bar{\mathbf{F}}^T \right), \quad (101)$$

and:

$$\begin{aligned} G_{\text{ext}} = & D\Pi_{\text{ext}} \cdot \boldsymbol{\eta} = \int_{\Omega} \mathbf{B} \cdot \boldsymbol{\eta} d\Omega \\ & + \int_{\partial_{\tau}\Omega} \bar{\mathbf{t}} \cdot \boldsymbol{\eta} d\Gamma. \end{aligned} \quad (102)$$

In the same manner, considering the variations ψ and q , respectively, in θ and p results in the following equations:

$$H = D\Pi \cdot \psi = \int_{\Omega} \psi [U'(\theta) - p] d\Omega = 0, \quad (103)$$

$$\Gamma = D\Pi \cdot q = \int_{\Omega} q(J - \theta) d\Omega = 0. \quad (104)$$

The response of the system is obtained by requiring that Eqs. (100), (103) and (104) be satisfied in each time step. Eq. (100) is nonlinear and should be solved iteratively. For the i th iteration of a given time step, we can write

$$G^i + \delta G^{i+1} = 0, \quad (105)$$

where, considering another admissible variation such as $\Delta \mathbf{u}$ in φ and dropping the superindices for convenience, δG has the following form:

$$\begin{aligned} \delta G = & DG \cdot \Delta \mathbf{u} = \int_{\Omega} [\nabla(\Delta \mathbf{u}) \boldsymbol{\tau}] : (\nabla \boldsymbol{\eta}) d\Omega \\ & + \int_{\Omega} (\nabla \boldsymbol{\eta}) : \left[pJ(\mathbf{1} \otimes \mathbf{1} - 2\mathbf{I}) + \mathbf{a}^{\text{dev}} \right] \\ & : \nabla(\Delta \mathbf{u}) d\Omega + \int_{\Omega} Dp \cdot \Delta \mathbf{u} J(\text{div} \boldsymbol{\eta}) d\Omega, \end{aligned} \quad (106)$$

with:

$$\mathbf{a}^{\text{dev}} = \mathbf{a}^{\text{dev, tr}} + \mathbf{a}^{\text{dev, cr}}, \quad (107)$$

which is the elastoplastic tangent moduli derived in previous section.

In Eq. (106), the first integral emerges as a result of geometric change in the body and leads to geometric stiffness matrix. The term containing \mathbf{a}^{dev} corresponds to material nonlinearity, and the material stiffness matrix derives from this term. The last integral represents the contribution due to change in pressure and is specially treated in the following section to avoid shear locking.

5.2. Mixed finite element formulation

We follow the methodology in [35,20,34] to construct finite element approximations for pressure p and dilatation θ . The resulting fields are discontinuous over elements, and can be effectively eliminated at element level to yield a generalized displacement model.

The following interpolations are considered for p and θ and their variations q and ψ within a typical finite element e .

$$p_e^h = \mathbf{\Gamma}^T \bar{\mathbf{p}} \quad \text{and} \quad q_e^h = \mathbf{\Gamma}^T \bar{\mathbf{q}}, \tag{108}$$

$$\theta_e^h = \mathbf{\Gamma}^T \bar{\theta} \quad \text{and} \quad \psi_e^h = \mathbf{\Gamma}^T \bar{\psi}, \tag{109}$$

where $\mathbf{\Gamma}$ is the vector of interpolation functions, and $\bar{\mathbf{p}}$, $\bar{\mathbf{q}}$, $\bar{\theta}$ and $\bar{\psi}$ are the vectors of nodal values, respectively, for p , q , θ and ψ .

Substituting Eqs. (108) and (109) into Eqs. (103) and (104), and performing straightforward manipulations, we get:

$$p_e^h = \mathbf{\Gamma}^T \mathbf{H}^{-1} \left[\int_{\Omega_e} \mathbf{\Gamma} U'(\theta_e^h) d\Omega_e \right], \tag{110}$$

$$\theta_e^h = \mathbf{\Gamma}^T \mathbf{H}^{-1} \left[\int_{\Omega_e} \mathbf{\Gamma} J_e^h d\Omega_e \right], \tag{111}$$

with:

$$\mathbf{H} = \int_{\Omega_e} \mathbf{\Gamma} \mathbf{\Gamma}^T d\Omega_e. \tag{112}$$

Eq. (110) along with Eq. (111) results in the following equation for the derivative of p_e^h in the direction $\Delta \mathbf{u}$:

$$Dp_e^h \cdot \Delta \mathbf{u} = \mathbf{\Gamma}^T \mathbf{H}^{-1} \left[\int_{\Omega_e} \mathbf{\Gamma} U''(\theta_e^h) \theta_e^h \overline{\text{div}}(\Delta \mathbf{u}) d\Omega_e \right], \tag{113}$$

where:

$$\overline{\text{div}}(\Delta \mathbf{u}) = \frac{1}{\theta_e^h} \mathbf{\Gamma}^T \mathbf{H}^{-1} \left[\int_{\Omega_e} \mathbf{\Gamma} J_e^h \text{div}(\Delta \mathbf{u}) d\Omega_e \right]. \tag{114}$$

Substitution of Eq. (113) into the last integral of Eq. (106) leads to:

$$\int_{\Omega_e} Dp \cdot \Delta \mathbf{u} J(\text{div} \boldsymbol{\eta}) d\Omega_e = \int_{\Omega_e} U''(\theta_e^h) \theta_e^h \overline{\text{div}}(\boldsymbol{\eta}) \theta_e^h \overline{\text{div}}(\Delta \mathbf{u}) d\Omega_e. \tag{115}$$

6. Numerical examples

In this section, numerical examples are presented to assess the performance of proposed algorithm. Error graphs are used to provide a measure for the accuracy of algorithm compared with backward Euler method. The employed solution procedure is the full Newton-Raphson scheme. In order to preserve the quadratic rate of convergence, it is essential to use consistent tangent moduli.

The form chosen for the volumetric part of the free energy, i.e. for the function $U(J)$ in Eq. (1), is:

$$U(J) = \frac{1}{2} \kappa \left[\frac{1}{2} (J^2 - 1) - \ln J \right], \tag{116}$$

where κ is the bulk modulus. As it is evident from the following expressions, a more general form is considered for nonlinear hardening in which a saturation term of exponential type is added to linear terms as well [11]:

$$K(\bar{e}^p) = \beta h(\bar{e}^p), \quad \beta \in [0, 1], \tag{117}$$

$$H(\bar{e}^p) = (1 - \beta) h(\bar{e}^p), \tag{118}$$

with:

$$h(\bar{e}^p) = \bar{K}_\infty - [\bar{K}_\infty - \bar{K}_0] \exp(-\delta \bar{e}^p) + \bar{H}' \bar{e}^p, \tag{119}$$

$$\delta > 0,$$

where \bar{K}_∞ , \bar{K}_0 , δ and \bar{H}' are material constants and β provides a modulation between pure kinematic hardening ($\beta = 0$) and pure isotropic hardening ($\beta = 1$). The value of α that is used to accomplish the numerical simulations is set to 0.50.

Four node quadrilateral elements with bilinear displacement interpolation along principal directions are employed in all numerical examples. Based on standard concepts in finite element analysis [36,37], the algorithm described in preceding sections is implemented into the ANIA (Automatic Nonlinear Incremental Analysis) program specially developed by the author for the solution of nonlinear problems.

Given a specified number of load steps, the error graphs are generated by comparing the output of algorithm with exact solution. Anticipating a prescribed tolerance, the exact solution can be obtained by solving the problem using a very fine time step such that a smaller time step does not change the solution. The following equation is used to compute the error percentage compared with exact solution:

$$E = \frac{|Q - Q_{ex}|}{Q_{ex}} \times 100, \tag{120}$$

where E is the error in percent, Q is the desired quantity in which the error is to be computed and Q_{ex} is the corresponding quantity from the exact solution.

6.1. Necking of a circular bar

This example is experimentally well documented in the literature and concerns the necking of a circular bar with a radius of 6.413 mm and length of 53.334 mm subject to uniaxial tension. The example is solved by many authors [38,25,39] and is used as benchmark to compare the results with the proposed algorithm. Material properties of the bar are shown in Table 1.

Due to the symmetry of problem, only one quarter of the bar is modeled using 200 axisymmetric elements. The finite element model, and the deformation of bar after 14 mm elongation are shown in Figure 2. The contours for Cauchy stress components, σ_{11} and σ_{22} , are shown in Figure 3. They are in good agreement with those reported by Simo [25]. The graphs of total load being applied to the bar versus the displacement are provided in Figures 4 and 5, respectively, for backward Euler method and the proposed algorithm.

Table 1. Material properties for circular bar.

Elastic modulus E	206.9 GPa
Poisson ratio ν	0.29
Residual flow stress \bar{K}_∞	0.715 GPa
Initial flow stress \bar{K}_0	0.45 GPa
Saturation exponent δ	16.93
Linear hardening coefficient \bar{H}'	0.12924 GPa
Isotropic hardening β	1.0

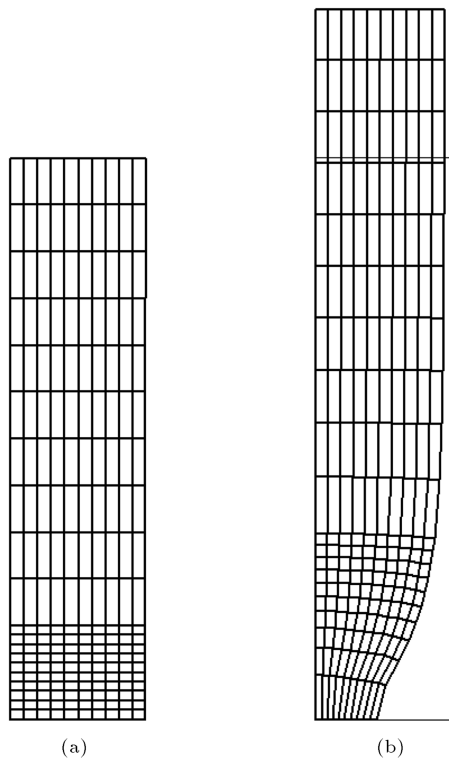


Figure 2. Necking of a circular bar: (a) Finite element model; and (b) deformation after 14 mm elongation.

Using the minimum number of load steps for backward Euler method, the graph in Figure 6 presents the error in computed total load for both algorithms.

To have an idea of computational effort, it should be mentioned that the number of load steps used to

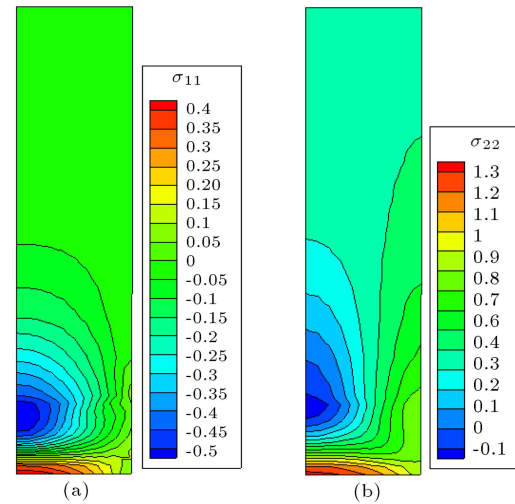


Figure 3. Necking of a circular bar. Contours of Cauchy stress components: (a) σ_{11} ; and (b) σ_{22} .

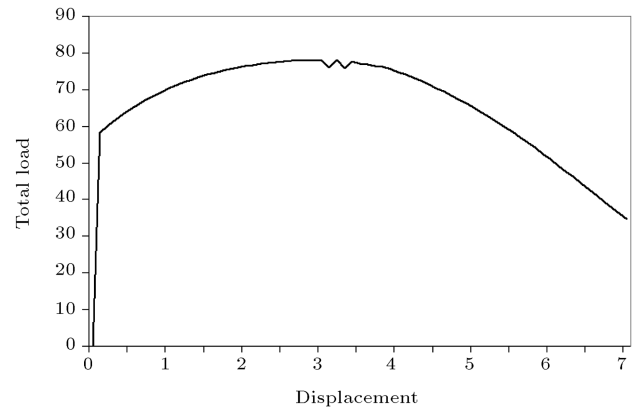


Figure 4. Necking of a circular bar. Load-displacement curve for backward Euler method.

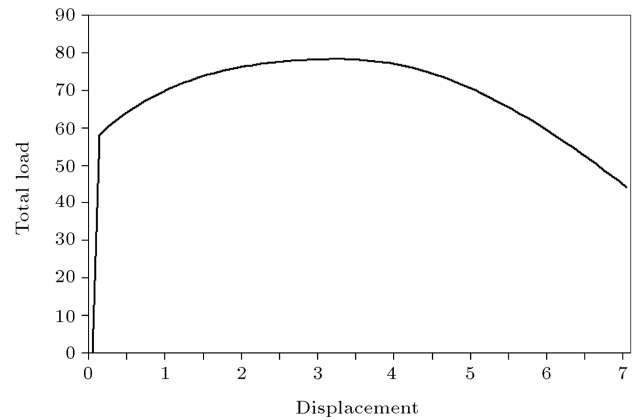


Figure 5. Necking of a circular bar. Load-displacement curve for the proposed algorithm.

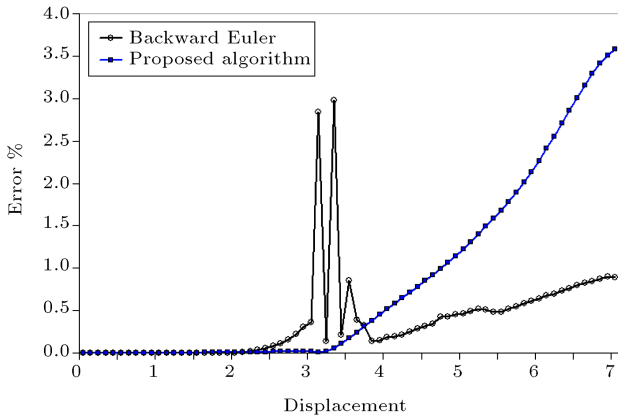


Figure 6. Necking of a circular bar. Error in total load for backward Euler method and the proposed algorithm.

solve the problem using the proposed algorithm is one sixth of the minimum number of load steps that is required for backward Euler method to converge. Moreover, a comparison between Figures 4 and 5 shows that about elongation 3 mm, where the necking is beginning to form, we have numerical problems for backward Euler method (oscillations about the peak of the curve) while the curve for the proposed algorithm is smooth showing that the algorithm is very stable from numerical point of view.

The exact solution used to generate the error graphs in Figure 6 is obtained from the application of the proposed algorithm employing very fine time steps. The backward Euler method could not be used because the oscillations about the peak of the load-displacement curve (see Figure 4) are not eliminated even with very small time steps. With larger time steps the aforementioned oscillations become so severe that the overall Newton-Raphson iterations cease to converge. The error graph for backward Euler method clearly shows that the stiffness matrix is ill-conditioned at the point where the necking is being formed. In contrast to backward Euler method, the error graph for the proposed algorithm is very smooth showing that the error increases uniformly (without oscillations) from the point where the necking begins to form toward the end of the loading program. In fact, there is no ill-conditioning problem with the stiffness matrix, and as the number of load steps is increased, the accuracy of the solution is improved. Moreover, the maximum error is 3.6% (versus 3.0% for backward Euler method) which is quite acceptable.

6.2. Expansion of a thick-walled cylinder

This example has been solved numerically in [25,40]. A thick-walled cylinder with an inner and outer radii of 10 and 20 units is under the action of an internal pressure. The inner radius is driven to a value of 85 units. Material properties chosen to replicate a rigid-plastic behavior are shown in Table 2. The axisymmetric

Table 2. Material properties for thick-walled cylinder.

Elastic modulus E	11050.0 MPa
Poisson ratio ν	0.454
Residual flow stress \bar{K}_∞	0.5 MPa
Initial flow stress \bar{K}_0	0.5 MPa
Saturation exponent δ	0.0
Linear hardening coefficient \bar{H}'	0.0
Isotropic hardening β	1.0

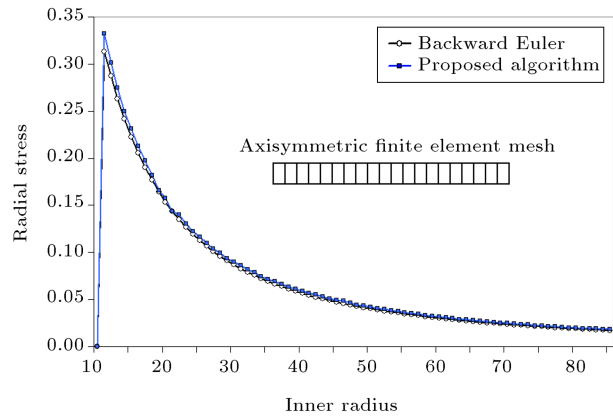


Figure 7. Expansion of a thick-walled cylinder. Finite element mesh and radial stress component, σ_{rr} , at inner radius for backward Euler method and the proposed algorithm.

mesh that is used to model the cylinder is shown in Figure 7 and consists of 20 4-node quadrilateral elements.

A graph of the radial Cauchy stress, σ_{rr} , at inner boundary versus the inner radius is provided in Figure 7 both for backward Euler method and the proposed algorithm. It is observed that the results of the proposed algorithm are in good agreement with backward Euler method. To give an idea of computational effort, it should be noted that the solution using the proposed algorithm is accomplished in one fifth the minimum number of load steps required for backward Euler method.

The graphs in Figure 8 present the error in computed radial stress component, σ_{rr} , at inner radius for both algorithms. The minimum number of load steps required for the convergence of backward Euler method is used to generate the graphs. The exact solution is obtained from the application of backward Euler method with very fine time steps. The maximum error in the solution from the proposed algorithm is 2.2% while the one from backward Euler method is 5.5%. The relatively higher error in backward Euler method in the initial stages of loading is due to the fact that it misses the point where the material begins to plasticize while this is not the case for the proposed algorithm.

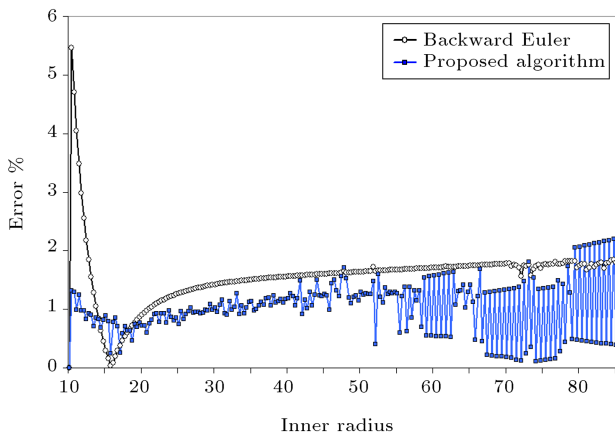


Figure 8. Expansion of a thick-walled cylinder. Error in radial stress component, σ_{rr} , at inner radius for backward Euler method and the proposed algorithm.

Table 3. Material properties for thick-wall sphere.

Elastic modulus E	800.0 MPa
Poisson ratio ν	0.3333
Residual flow stress \bar{K}_∞	0.486 MPa
Initial flow stress \bar{K}_0	0.083 MPa
Saturation exponent δ	0.75
Linear hardening coefficient \bar{H}'	0.0
Isotropic hardening β	1.0

6.3. Finite expansion of a thick-wall sphere

This example has been considered in [25,41]. Material properties are shown in Table 3. The sphere is modeled using 72 4-node quadrilateral elements. The initial and deformed meshes are shown in Figure 9. The graph in Figure 10 shows the variation of internal pressure versus internal radius both for backward Euler method and the proposed algorithm. Using the minimum number of load steps required for the convergence of backward Euler method, the graphs in Figure 11 present the error in computed internal pressure for both algorithms.

The same number of load steps is used to generate the curves in Figure 10. However, the backward Euler

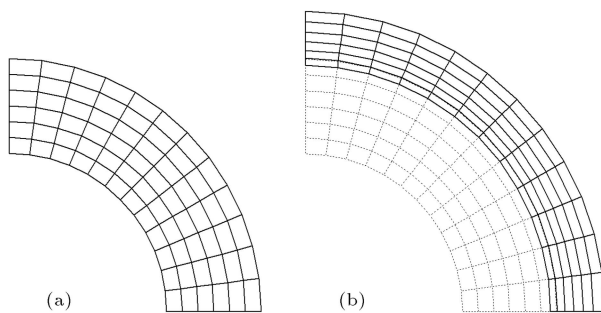


Figure 9. Finite expansion of a thick-walled sphere: (a) Initial finite element mesh; and (b) deformed mesh corresponding to final configuration.

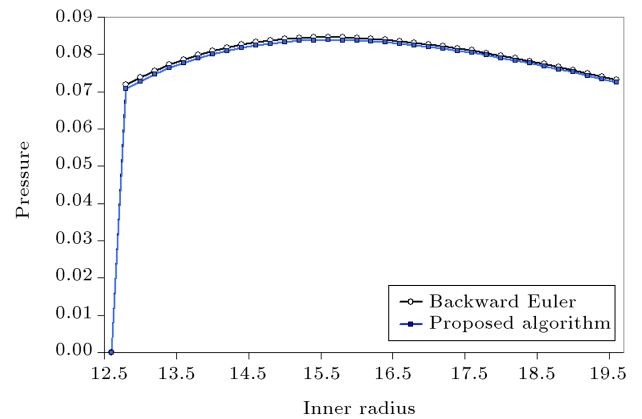


Figure 10. Finite expansion of a thick-walled sphere. Radial stress component, σ_{rr} , at inner radius for backward Euler method and the proposed algorithm.

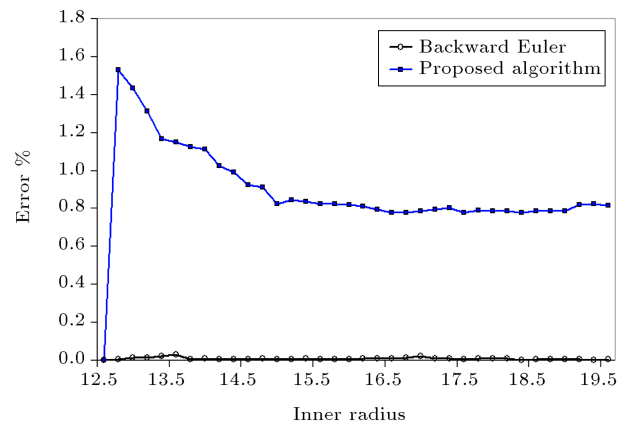


Figure 11. Finite expansion of a thick-walled sphere. Error in radial stress component, σ_{rr} , at inner radius for backward Euler method and the proposed algorithm.

method does not converge due to excessive element distortions when the number of load steps is lower than a certain limit while this limit is much smaller for the proposed algorithm and as the number of load steps is increased the results are monotonically improved. Regarding the error graphs in Figure 11, it is observed that the maximum error for the proposed algorithm is only 1.5%, although that of the backward Euler method is much smaller (about 0.03%). It seems that this is an easy problem for both algorithms.

6.4. Upsetting of an axisymmetric disk

This problem has been considered as a benchmark example by many authors [42,25,43]. An axisymmetric disk is upset to 26.67%. Material properties are given in Table 4. The disk is modeled using 100 4-node quadrilateral elements. A node-to-node Hertzian contact element is employed to simulate the subsequent contact between the machine piece and the disk.

The initial finite element mesh and the deformed mesh corresponding to final configuration are shown in Figure 12. The graph of total load being applied

Table 4. Material properties for axisymmetric disk.

Elastic modulus E	1000.0 MPa
Poisson ratio ν	0.3
Residual flow stress \bar{K}_∞	1.0 MPa
Initial flow stress \bar{K}_0	1.0 MPa
Saturation exponent δ	0.0
Linear hardening coefficient \bar{H}'	3.0 MPa
Isotropic hardening β	1.0

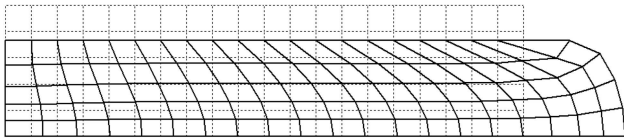


Figure 12. Upsetting of an axisymmetric disk. Initial mesh and deformed mesh corresponding to 26.67% deformation.

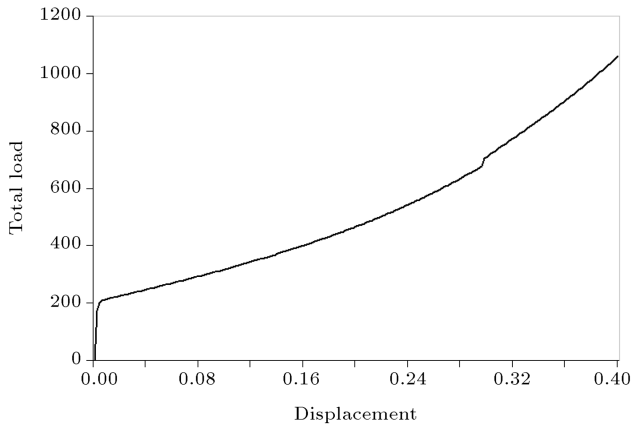


Figure 13. Upsetting of an axisymmetric disk. Load-displacement curve for backward Euler method and the proposed algorithm.

to the disk versus vertical displacement is shown in Figure 13 for backward Euler method and the proposed algorithm. Practically identical curves are obtained for both methods, however the number of load steps to accomplish the solution using the proposed algorithm is half of the minimum load steps required for backward Euler method to converge.

The graphs in Figure 14 present the error in computed total load for both algorithms. The minimum number of load steps for backward Euler method is used to generate the graphs. The exact solution is obtained by the application of backward Euler method with very fine time steps. Regarding this figure, it is observed that at all points, except the one at which the subsequent contact occurs between the machine piece and disk (approximately at displacement 0.298), the error for the proposed algorithm is less than 0.5%. Only at this point the error is higher than the maximum error for backward Euler method (2.6% versus 1.2%). From

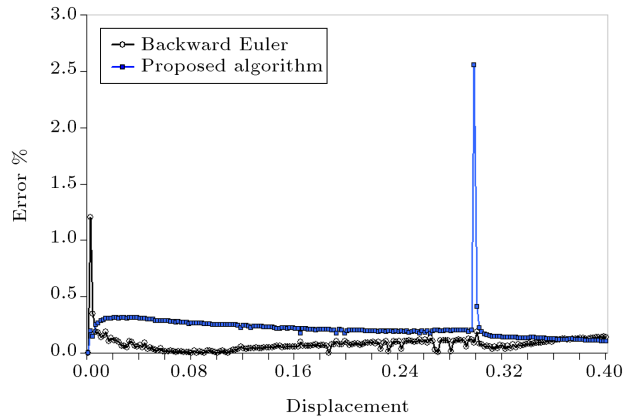


Figure 14. Upsetting of an axisymmetric disk. Error in total load for backward Euler method and the proposed algorithm.

Table 5. Material properties for axisymmetric billet.

Elastic modulus E	200.0 MPa
Poisson ratio ν	0.3
Residual flow stress \bar{K}_∞	0.3 MPa
Initial flow stress \bar{K}_0	0.3 MPa
Saturation exponent δ	0.0
Linear hardening coefficient \bar{H}'	0.7 MPa
Isotropic hardening β	1.0

the figure, it can also be inferred that the maximum error for backward Euler method at initial stages of loading is attributable to the fact that it misses the actual point where the material begins to plasticize. However, the proposed algorithm is capable to capture the onset of plasticizing.

6.5. Elastic-plastic upsetting of an axisymmetric billet

This example is considered as a severe test problem and is solved by many authors [25,41,43]. The initial radius and height of billet are 10 and 30 mm, respectively, and it is upset to 70% (versus 64% in previous works). Material properties are given in Table 5. Due to the obvious symmetry, only one quarter of specimen is modeled using 56 4-node quadrilateral elements. Node-to-node Hertzian contact elements are used to simulate the subsequent contacts between the machine piece and the billet.

The initial finite element mesh and the deformed mesh corresponding to final configuration are shown in Figure 15. The graph of total load being applied to billet versus vertical displacement is shown in Figure 16 for backward Euler method and the proposed algorithm. Similar to the previous example, identical curves are obtained for both methods. However, the number of load steps using the proposed algorithm is half of the minimum load steps required for backward Euler method.

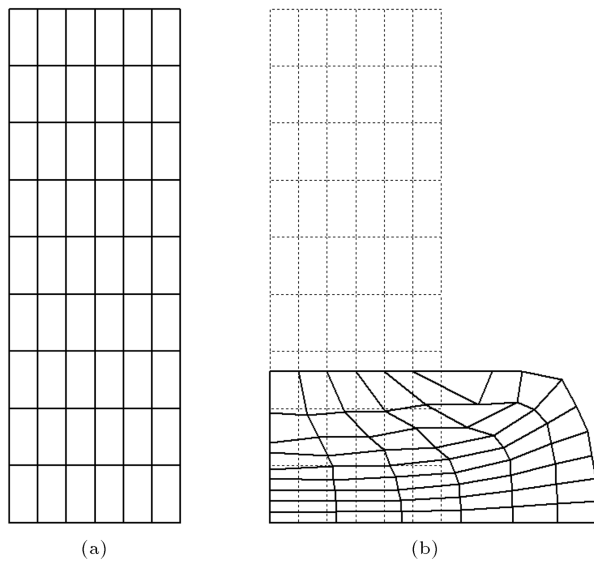


Figure 15. Elastic-plastic upsetting of an axisymmetric billet: (a) Initial mesh; and (b) deformed mesh corresponding to 70% upsetting.

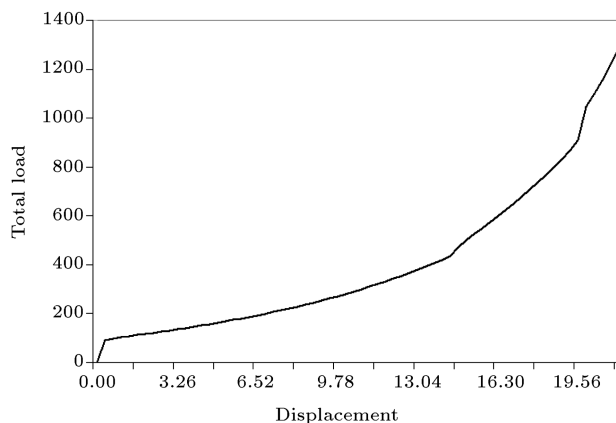


Figure 16. Elastic-plastic upsetting of an axisymmetric billet. Load-displacement curve for backward Euler method and the proposed algorithm.

The graphs in Figure 17 present the error in computed total load for both algorithms and are generated using the minimum number of load steps that is required for backward Euler method to converge. The exact solution is obtained by the application of backward Euler method with very fine time steps. Regarding the figure, it is observed that the maximum error for the proposed algorithm is 4.9% while for backward Euler method it is 19.5%. Moreover, the error for the proposed algorithm is less than backward Euler method at all points. For example, at points where subsequent contacts occur between the machine piece and billet (respectively at displacements 14.67 mm and 19.87 mm), the error for the proposed algorithm is 1.6% and 1.1%. The corresponding values for backward Euler method are 6.7% and 2.9%. The maximum error for backward Euler method is

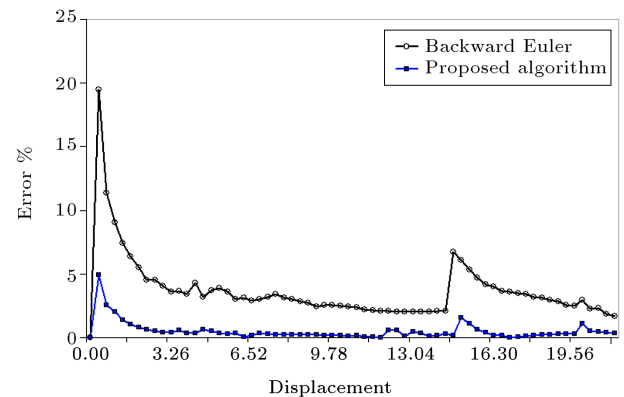


Figure 17. Elastic-plastic upsetting of an axisymmetric billet. Error in total load for backward Euler method and the proposed algorithm.

attributed to the point where the material begins to plasticize.

7. Conclusions

Inspired by midpoint rule algorithms in small deformation plasticity, a novel integration algorithm was developed in this work for finite strain J_2 plasticity. The formulation of algorithmic setup as well as the trial and stress correction steps were discussed in detail. Having computed the key parameters, the stress tensor is derived from the corresponding potential and therefore the hyperelastic nature of algorithm is preserved at all configurations. This property can be enumerated as one of the main features of algorithm. The proposed integration scheme is amenable to closed-form linearization and the formulation of consistent tangent operator was provided as well.

Through the solution of benchmark examples, it was shown that the algorithm is very stable from the numerical point of view. In other words, the backward Euler algorithm is very sensitive to the size of time step and if it is larger than a certain limit the algorithm ceases to converge due to excessive element distortions. This is in contrast to the observed behavior of the proposed algorithm which provides the capability of using large time steps. If the size of time step is too large, merely an approximate solution is obtained which is improved with smaller time steps but the algorithm does not diverge or stop due to element distortions. In all numerical simulations, it was observed that using the same number of load steps, as for backward Euler method, the maximum error in the solution obtained by the proposed algorithm is less than 5% which is quite satisfactory.

References

1. Wilkins, M.L. "Calculation of elastic-plastic flow", In *Methods in Computational Physics*, B. Adler, Ed., **3**,

- pp. 211-263, Academic Press, New York (1964).
2. Ortiz, M. and Popov, E.P. "Accuracy and stability of integration algorithms for elastoplastic constitutive relations", *Int. J. Numer. Methods Eng.*, **21**, pp. 1561-1576 (1985).
 3. Ortiz, M. and Simo, J.C. "An analysis of a new class of integration algorithms for elastoplastic constitutive equations", *Int. J. Numer. Methods Eng.*, **23**, pp. 353-366 (1986).
 4. Simo, J.C. "Topics on the numerical analysis and simulation of plasticity", In *Handbook of Numerical Analysis*, P.G. Ciarlet and J.L. Lions, Eds., **6**, pp. 179-499, Elsevier, Amsterdam (1998).
 5. Artioli, E., Auricchio, F. and Beirão da Veiga, L. "Generalized midpoint integration algorithms for J_2 plasticity with linear hardening", *Int. J. Numer. Methods Eng.*, **72**, pp. 422-463 (2007).
 6. Jahanshahi, M. "Second order integration algorithms for J_2 plasticity with generalized isotropic/kinematic hardening", *Asian J. Civil Eng.*, **13**(2), pp. 203-232 (2012).
 7. Jahanshahi, M. "Numerical assessment of a double step integration algorithm for J_2 plasticity with Armstrong-Frederick evolution of back stress", *Sci. Iran. Trans. A*, **19**(5), pp. 1168-1179 (2012).
 8. Ellsiepen, P. and Hartmann, S. "Remarks on the interpretation of current non-linear finite element analyses as differential-algebraic equations", *Int. J. Numer. Methods Eng.*, **51**, pp. 679-707 (2001).
 9. Hartmann, S. "A remark on the application of the Newton-Raphson method in non-linear finite element analysis", *Comput. Mech.*, **36**, pp. 100-116 (2005).
 10. Hartmann, S., Quint, K.J. and Arnold, M. "On plastic incompressibility within time-adaptive finite elements combined with projection techniques", *Comput. Methods Appl. Mech. Eng.*, **198**, pp. 178-193 (2008).
 11. Simo, J.C. and Hughes, T.J.R., *Computational Inelasticity*, Springer, New York (1998).
 12. de Souza Neto, E.A., Perić, D. and Owen, D.R.J., *Computational Methods for Plasticity: Theory and Applications*, John Wiley & Sons, New York (2008).
 13. Goudreau, G.L. and Hallquist, J.O. "Recent developments in large-scale finite element Lagrangian hydrocode technology", *Comput. Methods Appl. Mech. Eng.*, **33**, pp. 725-757 (1982).
 14. Hallquist, J.O. "NIKE 2D: An implicit, finite deformation, finite element code for analyzing the static and dynamic response of two dimensional solids", Report UCRL-52678, Lawrence Livermore National Laboratories, University of California, Livermore (1979).
 15. Hallquist, J.O. "DYNA 3D: An explicit finite element code for dynamic analysis in three dimensions", Report, Lawrence Livermore National Laboratories, University of California, Livermore (1988).
 16. Key, S.W. "HONDO - A finite element computer program for the large deformation response of axisymmetric solids", Report 74-0039, Sandia National Laboratories, Albuquerque, New Mexico (1974).
 17. Key, S.W., Stone, C.M. and Krieg, R.D. "Dynamic relaxation applied to the quasi-static, large deformation, inelastic response of axisymmetric solids", In *Nonlinear Finite Element Analysis in Structural Mechanics*, W. Wunderlich, E. Stein and K.J. Bathe, Eds., Springer, Berlin (1981).
 18. Nagtegaal, J.C. and Veldpaus, F.E. "On the implementation of finite strain plasticity equations in a numerical model", In *Numerical Analysis of Forming Processes*, J.F.T. Pittman, O.C. Zienkiewicz, R.D. Wood and J.M. Alexander, Eds., pp. 351-371, John Wiley & Sons, New York (1984).
 19. Rolph, W.D. and Bathe, K.J. "On a large strain finite-element formulation for elasto-plastic analysis", In *Constitutive Equations: Macro and Computational Aspects*, K.J. Willam, Ed., pp. 131-147, AMD, ASME, New York (1984).
 20. Simo, J.C. "A framework for finite strain elastoplasticity based on maximum plastic dissipation and the multiplicative decomposition: Part I. Continuum formulation", *Comput. Methods Appl. Mech. Eng.*, **66**, pp. 199-219 (1988).
 21. Lee, E.H. "Elastic-plastic deformations at finite strains", *J. Appl. Mech.*, **36**, pp. 1-6 (1969).
 22. Nemat-Nasser, S. "On finite deformation elastoplasticity", *Int. J. Solids Struct.*, **18**, pp. 857-872 (1982).
 23. Lee, E.H. and Liu, D.T. "Finite strain elastic-plastic theory particularly for plane wave analysis", *J. Appl. Phys.*, **38**, pp. 19-27 (1967).
 24. Simo, J.C. "On the computational significance of the intermediate configuration and hyperelastic stress relations in finite deformation elastoplasticity", *Mech. Mater.*, **4**, pp. 439-451 (1985).
 25. Simo, J.C. "A framework for finite strain elastoplasticity based on maximum plastic dissipation and the multiplicative decomposition: Part II. Computational aspects", *Comput. Methods Appl. Mech. Eng.*, **68**, pp. 1-31 (1988).
 26. Simo, J.C. "Algorithms for static and dynamic multiplicative plasticity that preserve the classical return mapping schemes of the infinitesimal theory", *Comput. Methods Appl. Mech. Eng.*, **99**, pp. 61-112 (1992).
 27. Perić, D. and de Souza Neto, E.A. "A new computational model for Tresca plasticity at finite strains with an optimal parametrization in the principal space", *Comput. Methods Appl. Mech. Eng.*, **171**, pp. 463-489 (1999).
 28. Eterovic, A.L. and Bathe, K.J. "A hyperelastic-based large strain elasto-plastic constitutive formulation with combined isotropic-kinematic hardening using the logarithmic stress and strain measure", *Int. J. Numer. Methods Eng.*, **30**, pp. 1099-1114 (1990).

29. Dafalias, Y.F. “Plastic spin: Necessity or redundancy”, *Int. J. Plasticity*, **14**(9), pp. 909-931 (1998).
30. Haupt, P. “On the concept of an intermediate configuration and its application to a representation of viscoplastic-plastic material behavior”, *Int. J. Plasticity*, **1**, pp. 303-316 (1985).
31. Lubliner, J. “Normality rules in large-deformation plasticity”, *Mech. Mater.*, **5**, pp. 29-34 (1986).
32. Dafalias, Y.F. “The plastic spin”, *J. Appl. Mech.*, **52**, pp. 865-871 (1986).
33. Carlson, D.E. and Hoger, A. “The derivative of a tensor-valued function of a tensor”, *Quart. Appl. Math.*, **44**(3), pp. 409-423 (1986).
34. Simo, J.C. and Taylor, R.L. “Quasi-incompressible finite elasticity in principal stretches. Continuum basis and numerical algorithms”, *Comput. Methods Appl. Mech. Eng.*, **85**, pp. 273-310 (1991).
35. Nagtegaal, J.C., Parks, D.M. and Rice, J.R. “On numerically accurate finite element solutions in the fully plastic range”, *Comput. Methods Appl. Mech. Eng.*, **4**, pp. 153-177 (1974).
36. Bathe, K.J., *Finite Element Procedures*, Prentice-Hall, New York (1996).
37. Zienkiewicz, O.C. and Taylor, R.L., *The Finite Element Method*, McGraw-Hill, New York (2002).
38. Montáns, F.J. and Bathe, K.J. “Computational issues in large strain elasto-plasticity: An algorithm for mixed hardening and plastic spin”, *Int. J. Numer. Methods Eng.*, **63**, pp. 159-196 (2005).
39. Simo, J.C. and Armero, F. “Geometrically non-linear enhanced strain mixed methods and the method of incompatible modes”, *Int. J. Numer. Methods Eng.*, **33**, pp. 1413-1449 (1992).
40. Simo, J.C. and Ortiz, M. “A unified approach to finite deformation elastoplastic analysis based on the use of hyperelastic constitutive equations”, *Comput. Methods Appl. Mech. Eng.*, **49**, pp. 221-245 (1985).
41. Simo, J.C., Taylor, R.L. and Pister, K.S. “Variational and projection methods for the volume constraint in finite deformation elastoplasticity”, *Comput. Methods Appl. Mech. Eng.*, **51**, pp. 177-208 (1985).
42. Nagtegaal, J.C. and De Jong, J.E. “Some computational aspects of elastic-plastic large strain analysis”, *Int. J. Numer. Methods Eng.*, **17**, pp. 15-41 (1981).
43. Taylor, L.M. and Becker, E.B. “Some computational aspects of large deformation, rate-dependent plasticity problems”, *Comput. Methods Appl. Mech. Eng.*, **41**(3), pp. 251-278 (1983).

Biography

Mohsen Jahanshahi received his BS in civil engineering from Shahid Bahonar University, Kerman. He completed his MS and PhD studies in Structural Engineering at Iran University of Science and Technology, Tehran. Currently he is an assistant professor in the Department of Civil Engineering, School of Science and Engineering, Sharif University of Technology, International Campus, Kish Island, Iran.